The Journal of
Chemical Physics

Vibronic and excitonic dynamics in perylenediimide dimers and tetramer

Cite as: J. Chem. Phys. **153**, 224101 (2020); https://doi.org/10.1063/5.0024530
Submitted: 08 August 2020 . Accepted: 11 November 2020 . Published Online: 08 December 2020

Ivo H. M. van Stokkum, Chanelle C. Jumper, Tia S. Lee, Mykhaylo Myahkostupov, Felix N. Castellano, and Gregory D. Scholes

The Journal of Chemical Physics ARTICLE scitation.org/journal/jcp

Vibronic and excitonic dynamics in perylenediimide dimers and tetramer

Cite as: J. Chem. Phys. 153, 224101 (2020); doi: 10.1063/5.0024530
Submitted: 8 August 2020 • Accepted: 11 November 2020 •
Published Online: 8 December 2020

Ivo H. M. van Stokkum,[1,a)] Chanelle C. Jumper,[2] Tia S. Lee,[3] Mykhaylo Myahkostupov,[3] Felix N. Castellano,[3] and Gregory D. Scholes[4]

AFFILIATIONS

[1] Institute for Lasers, Life and Biophotonics, Faculty of Sciences, Vrije Universiteit Amsterdam, De Boelelaan 1081, 1081 HV Amsterdam, The Netherlands
[2] Department of Chemical and Biological Engineering, Princeton University, Princeton, New Jersey 08544, USA
[3] Department of Chemistry, North Carolina State University, Raleigh, North Carolina 27695-8204, USA
[4] Department of Chemistry, Princeton University, Princeton, New Jersey 08544, USA

Note: This paper is part of the JCP Special Topic on Excitons: Energetics and Spatio-temporal Dynamics.
[a)] **Author to whom correspondence should be addressed:** i.h.m.van.stokkum@vu.nl. **Telephone:** +31205987868

ABSTRACT

Broad-band pump–probe spectroscopy combined with global and target analysis is employed to study the vibronic and excitonic dynamics of two dimers and a tetramer of perylenediimides. A simultaneous analysis is developed for two systems that have been measured in the same conditions. This enhances the resolvability of the vibronic and excitonic dynamics of the systems, and the solvent contributions that are common in the experiments. We resolve two oscillations of 1399 cm^{-1} or 311 cm^{-1} damped with ≈30/ps involved in vibrational relaxation and two more oscillations of 537 cm^{-1} or 136 cm^{-1} damped with ≈3/ps. A relaxation process with a rate of 2.1/ps–3.2/ps that is positively correlated with the excitonic coupling was discovered in all three model systems, attributed to annihilation of the one but lowest exciton state.

INTRODUCTION

Light harvesting is the first step in natural photosynthesis.[1,2] In artificial photosynthesis,[3] bay substituted perylenediimides (PDIs) are versatile chromophores,[4,5] which are the building blocks of supramolecular complexes that mimic photosynthetic antennas.[6–11] Photosynthetic excitons play a crucial role in light harvesting.[12–14] There have been many studies of excitons in model few-chromophore systems and how exciton states influence the excited state dynamics.[15,16] Here, we focus on the analysis of vibronic wavepackets produced by ultrashort excitation of some model multichromophore systems. In particular, we further investigate the use of global and target analysis of the oscillations caused by wavepacket motion. Using this fitting method, we obtain more details about the wavepacket motion and its interplay with exciton states.

To obtain a better understanding of vibronic and excitonic dynamics, model excitonic systems that consist of a dimer or tetramer of PDI chromophores have been designed.[17–19] The complete line structures of the PDI dimers A and B and of the PDI tetramer studied here are shown in Fig. 1. The PDI dimers and tetramer are composed of identical PDI subunits bearing 1-hexylheptyl groups that were incorporated to enhance the solubility. The PDI subunits are linked by a diacetylene bridge (dimer A), by an acetylene bridge (dimer B), or by a methane-centered tetrahedral rigid core (tetramer). The distances between the PDI subunits in these three model excitonic systems differ and thus also their coupling strength. The tetramer has the cleanest exciton effect, since the tetramer has no through-conjugation of the chromophores.[18] The absorption spectrum of dimer A[19] shows molecular exciton splitting, indicating that excitation is delocalized. The 2D electronic spectroscopy study on dimer A[19] demonstrated that for this model

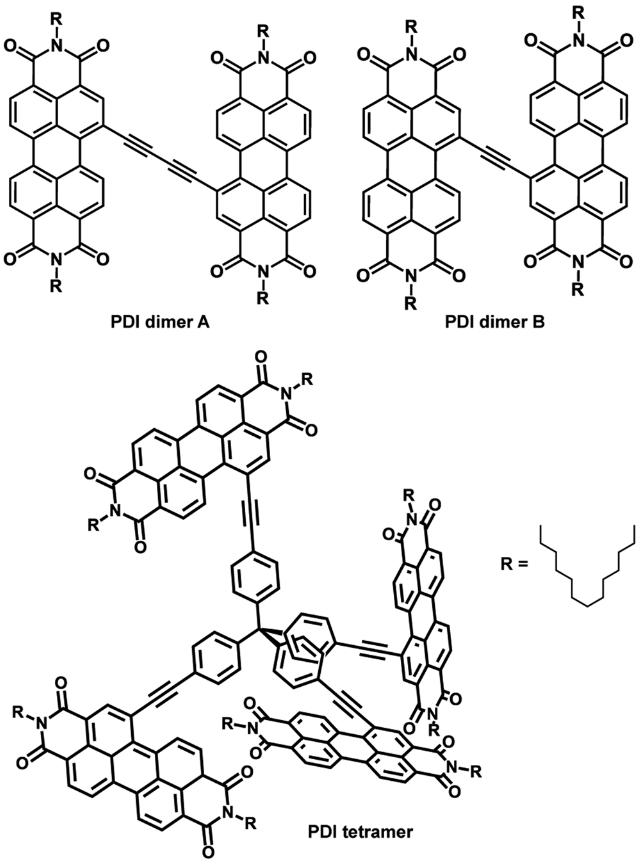

FIG. 1. Perylenediimide (PDI) dimer A, dimer B, and tetramer full line structures.

homodimer system in the strong electronic coupling regime, energy relaxation within the excitonic manifold occurs in the very early (<50 fs) time frame after photoexcitation, precluding the persistence of long-lived coherences between exciton states. It was proposed in Ref. 19 that intramolecular degrees of freedom dictate the relaxation rate through radiationless internal conversion pathways. In order to understand internal conversion mechanisms in systems with a Frenkel exciton electronic structure, we investigate the vibronic and excitonic dynamics by employing broad-band (BB) pump–probe spectroscopy combined with global and target analysis.[20–23] Thus, we can simultaneously achieve femtosecond time resolution over a large spectral range of 500 nm–680 nm. All BB experiments present very intense signals around zero delay, which are known as the "coherent artifact" (CA). Careful global and target analysis is employed here to resolve the CA contribution and the solvent contributions from the vibronic and excitonic dynamics of the model excitonic systems. To this end, we extend our global and target analysis methodology[22] to a simultaneous analysis of two excitonic systems measured in the same conditions. We ascribe the common vibrational features in the data to solvent contributions, which are the CA and long-lived oscillations resulting from off-resonance impulsive stimulated Raman scattering (ISRS).[24–26] These ISRS signals can be overwhelming,[27] thereby obscuring the signals resulting from the vibronic and excitonic dynamics. Therefore, in this study, a proper solvent has been chosen, chlorobenzene, which has less strong ISRS signals than the more commonly used dichloromethane.[27,28] The simultaneous analysis will be demonstrated to resolve four damped oscillations that can be attributed to the model excitonic systems.

MATERIALS AND METHODS

Sample

The complete line structures of the PDI dimers A and B and of the PDI tetramer are shown in Fig. 1. The synthesis and characterization have been described elsewhere.[17–19] The PDI dimer or tetramer was individually diluted in chlorobenzene to an optical density (OD) at the absorption maximum of 0.24 cm^{-1} for the transient absorption experiments.

Steady state measurements

Steady state absorption and emission measurements have been conducted in dichloromethane as described in Ref. 19.

Transient absorption measurements

Broadband transient absorption measurements have been described in Refs. 20–22. Detection was *parallel*, which includes depolarization effects. A typical experiment consists of nt = 1201 time-gated spectra measured at nλ = 584 wavelengths (with wavelength step 0.3 nm). Time-gated difference spectra were taken at equidistant time points for 1.2 ps (with a time step of 1 fs). To increase the signal to noise ratio (SNR), four consecutive wavelength points (corresponding to 1.2 nm) and two consecutive time points have been averaged. Each experiment was repeated five times to confirm reproducibility. Broadband excitation pulses were tuned centrally to 580 nm, overlapping with the low energy part of the absorption spectrum (indicated by, respectively, red and blue curves in Fig. S1).

Modeling and parameter estimation

The global and target analysis methodology has been elaborately described in Ref. 22. Briefly, the superposition model for the Time Resolved Spectra [$TRS(t,\lambda)$] is given by

$$TRS(t,\lambda) = \sum_{l=1}^{Nstates} c_l^S(t',\theta)SADS_l(\lambda) + \sum_{n=1}^{Nosc} DOAS_n(\lambda)\cos(\omega_n t' - \varphi_n(\lambda))\exp(-\gamma_n t').$$

The evolution of the ground and excited state vibrational wavepackets created by the short laser pulse is described with a superposition of damped oscillations. The amplitude of a damped oscillation $\cos(\omega_n t)\exp(-\gamma_n t)$ as a function of the detection wavelength constitutes a Damped Oscillation Associated Spectrum [$DOAS_n(\lambda)$] with an accompanying wavelength dependent phase $\varphi_n(\lambda)$. The measured TRS are modeled with the help of the following matrix formula:

$$TRS = C^S(\theta,\mu,\Delta)\cdot SADS^T + \mathrm{Cos}(\omega,\gamma,\mu,\Delta)\cdot A^T + \mathrm{Sin}(\omega,\gamma,\mu,\Delta)\cdot B^T + IRF(\mu,\Delta')\cdot IRFAS^T,$$

where the matrix $C^S(\theta, \mu, \Delta)$ contains in its columns the populations $c_l^S(t)$ of the compartmental model used. The matrix SADS contains in its columns the Species Associated Difference Spectra $[SADS_l(\lambda)]$. The matrices $\mathrm{Cos}(\omega, \gamma, \mu, \Delta)$ and $\mathrm{Sin}(\omega, \gamma, \mu, \Delta)$ contain in their columns the damped oscillations, and the matrices A and B comprise their amplitudes. In order to limit the number of free parameters, we assume wavelength independence of the eigenfrequency ω_n and of the damping rate γ_n. The final term, which describes the coherent artifact, contains a matrix $IRF(\mu, \Delta')$ with the zeroth, first, and second derivatives of the Instrument Response Function (IRF).[29] Experimentally, we found that the width $\Delta' > \Delta$, as will be discussed below. Associated with each IRF derivative are the columns of the *IRFAS* matrix. The SADS, A, B, and IRFAS matrices are conditionally linear parameters that are estimated with the help of the variable projection algorithm.[22,30] The CA is described by the $IRF(\mu, \Delta')\cdot IRFAS^T$ term plus a number of strongly damped oscillations, some of which are time-reversed to account for pre-zero oscillations due, for example, to pump-perturbed free induction decay.[31,32] The DOAS and phases cannot be fitted directly but must be computed from the estimated cosine and sine amplitude matrices A and B. The nth $DOAS_n$ at wavelength λ_j is computed as

$$DOAS_{jn} = \sqrt{A_{jn}^2 + B_{jn}^2}.$$

The reconstruction of the phase φ_n, called phase unwrapping, the parameter estimation, and the residual analysis have been described in Ref. 22.

When the compartmental model consists of independently decaying species, with populations $c_l^D(t, k_l, \mu, \Delta)$ (superscript D stands for decay), their spectra are termed $DADS_l(\lambda)$ (Decay Associated Difference Spectra). The interrelation between the DADS and SADS is expressed in the following matrix equation:[22]

$$C^D(\theta,\mu,\Delta)\cdot DADS^T = C^S(\theta,\mu,\Delta)\cdot SADS^T.$$

Here, the matrix $C^D(\theta, \mu, \Delta)$ contains in its lth column the decay $c_l^D(t, k_l, \mu, \Delta)$.

When two systems have been measured in the same conditions, they can be simultaneously analyzed. In this simultaneous analysis, the parameters describing what is common in the experiments can be linked, thus enhancing the resolvability of the vibronic and excitonic dynamics of the systems. The solvent contributions that are the CA and long-lived ISRS oscillations, which are common in the experiments, can thus be resolved more reliably. To aid the interpretation of the large amount of estimated parameters, it is instructive to synthesize the total CA contribution to the signal by adding the $IRF(\mu, \Delta')\cdot IRFAS^T$ term and the strongly damped oscillations that are ascribed to the CA. Likewise, a solvent ISRS signal can be synthesized by adding all the solvent ISRS oscillations. These syntheses allow us to judge the applicability of the methodology.

For the spectral decomposition, we employed a superposition of Gaussian bands,[30]

$$\varepsilon(\bar{\nu}) = \sum_{i=1}^{nbands} a_i \bar{\nu}^p \exp\left(-\ln(2)\left(2(\bar{\nu} - \bar{\nu}_{\max,i})/\Delta\bar{\nu}_i\right)^2\right),$$

with p equal to 5 or 1 for emission or (difference) absorption, respectively. Parameters a, $\bar{\nu}_{\max}$, and $\Delta\bar{\nu}$ are the amplitude, location of the maximum, Full Width at Half Maximum (FWHM) of a Gaussian band.

RESULTS AND DISCUSSION

Steady state spectra

The fluorescence properties of the PDI monomer, dimers A and B, and tetramer in dichloromethane are collated in Table I. The steady state absorption and emission spectra in dichloromethane are depicted in Fig. 2. Compared to the PDI monomer, which has a lowest absorption peak at 535 nm, the excitonic interaction is strongest in PDI dimer B, where the PDI moieties are closest, resulting in a lowest exciton absorption at 588 nm (red curve right most peak). In PDI dimer A, the excitonic interaction is still very strong, resulting in a lowest exciton absorption at ≈571 nm (green curve right most shoulder). In the PDI tetramer, the PDI moieties are further apart (Fig. 1) resulting in a smaller redshift to 550 nm. The maximum emission wavelength shows the same trend, with a shift of 30 nm for the PDI tetramer, and 55 nm and 75 nm for PDI dimers A and B, respectively (Table I, and Fig. 2). The steady state absorption and emission spectra in chlorobenzene of PDI dimer A and tetramer are very similar to those in dichloromethane (Fig. S2), but the maximum emission wavelengths are blue shifted by 5 nm and 2.5 nm (Table S1).

The linear absorption, fluorescence, and structures of PDI dimer A have earlier been reported in Ref. 19 together with the application of the exciton model. Based on the exciton model and the experimental linear absorption spectrum, an electronic coupling of 970 cm^{-1} and a dimerization shift of −480 cm^{-1} have been computed. In combination with the vibrational frequency of 1395 cm^{-1}, this places the PDI dimer in the complicated intermediate-strength vibronic coupling regime: the excitonic coupling, the vibrational quantum, and the relaxation energy are all of the same order of magnitude. It was concluded in Ref. 19 that there was partial agreement between the exciton model computation and the experimental spectra of PDI dimer A and that "there are evidently factors missing from the theory needed to model the spectra accurately, which will

TABLE I. Fluorescence lifetime, absolute quantum yield, and maximum emission wavelength of the PDI monomer, dimers A and B, and tetramer measured in dichloromethane.

PDI compound	τ_{FL} (ns)	Φ (AQY)	$\lambda_{\mathrm{max,em}}$ (nm)
Monomer	4.9	0.883	545
Dimer A	1.3	0.097	600
Dimer B	1.5	0.116	620
Tetramer	6.8	0.814	575

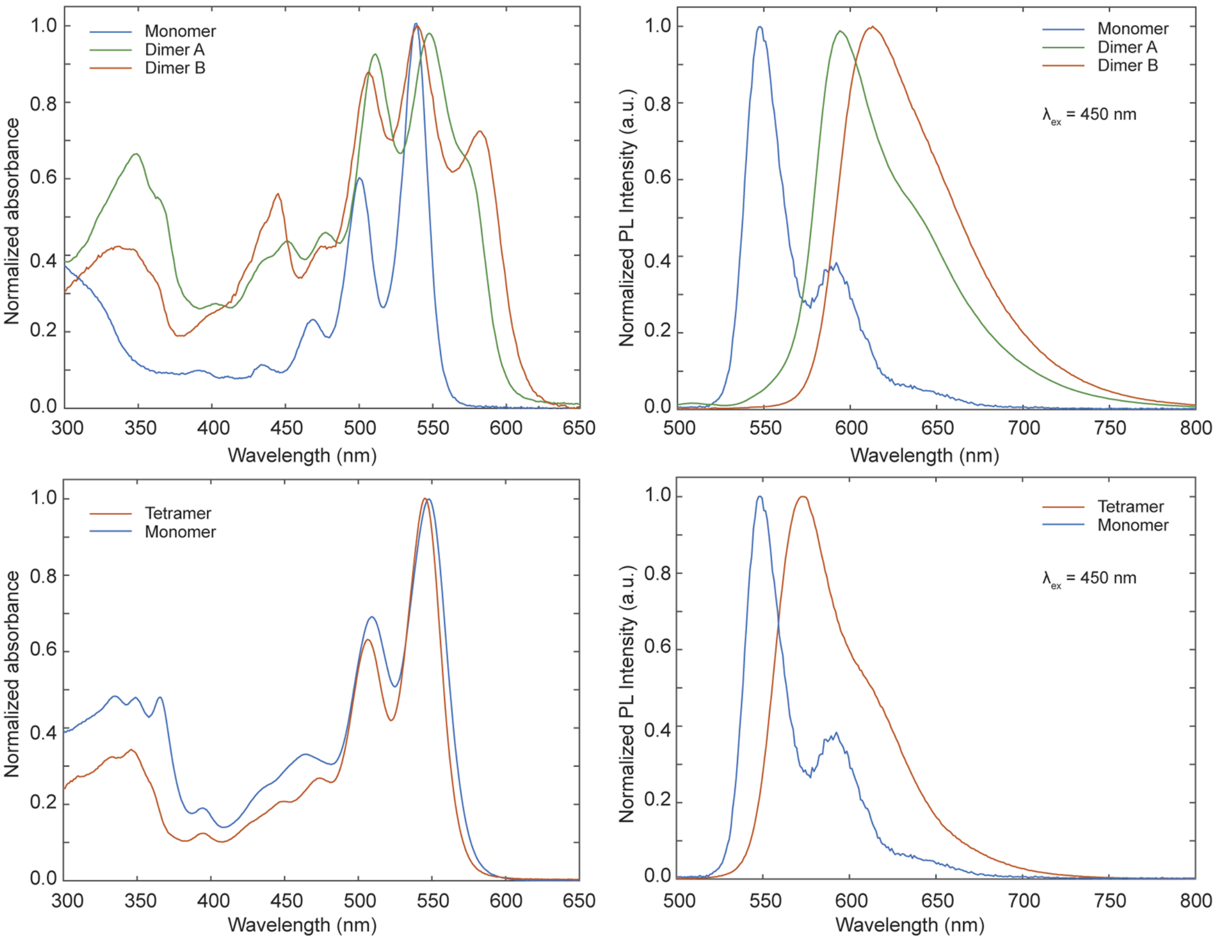

FIG. 2. Steady state absorption and emission spectra of the PDI monomer, dimers A and B, and tetramer measured in dichloromethane.

be the subject of future research." Below, we will perform a spectral decomposition of the steady state spectra of the tetramer, which has the cleanest exciton effect.

Target analysis of transient absorption spectra

Dimer B and tetramer

The broadband TA experiments in chlorobenzene solution have been performed with pulses centered at 580 nm. The amplitude of the coherent artifact plus damped oscillations is huge, with extrema straddling time zero near 100 mOD (Fig. S3). It is amazing that the PDI dimer B and the PDI tetramer data show virtually the same oscillatory pattern [Fig. 3(a) and Fig. S3]. Therefore, first, a simultaneous DOAS analysis of the PDI dimer B and the PDI tetramer data was attempted, assuming identical DOAS and IRFAS, but independent SADS. Next, the analysis was refined, allowing for four independent DOAS for dimer B and the tetramer. Thus, a final rms error of the fit was reached of 0.6 mOD, corresponding to a SNR better than 100 [Fig. 3(a), Figs. S3 and S4]. No obvious structure is discernible in the first left and right singular vectors of the residual matrix depicted in Fig. S5. This procedure allows us to confidently resolve the solvent contributions and the excitonic system contributions. Each excitonic system is described by two SADS or DADS [Figs. 3(b)–3(d)] and four DOAS [Figs. 3(e) and 3(f)]. In addition, the solvent contributions are described by the IRFAS (Fig. S6Q), five practically undamped DOAS (Nos. 1–5 in Figs. S6M–S6O), and six DOAS (Nos. 6–11) that are related to the fitting of the pre-zero oscillations and the CA, and will not be discussed further. The first undamped DOAS shows a node at 585 nm, accompanied by a ≈π-phase jump (black in Figs. S6N and S6O). This is in agreement with the off-resonance ISRS mechanism in which the generated ground state vibrational coherence modulates the refractive index of the medium, resulting in a periodic red- and blue-shift of the probe pulse spectrum.[24–26] Analogously, also the other four practically undamped DOAS (Nos. 2–5 in Figs. S6M–S6O) are assigned to ISRS from the chlorobenzene solvent, since 999 cm^{-1} corresponds to a well-known Raman band and also to

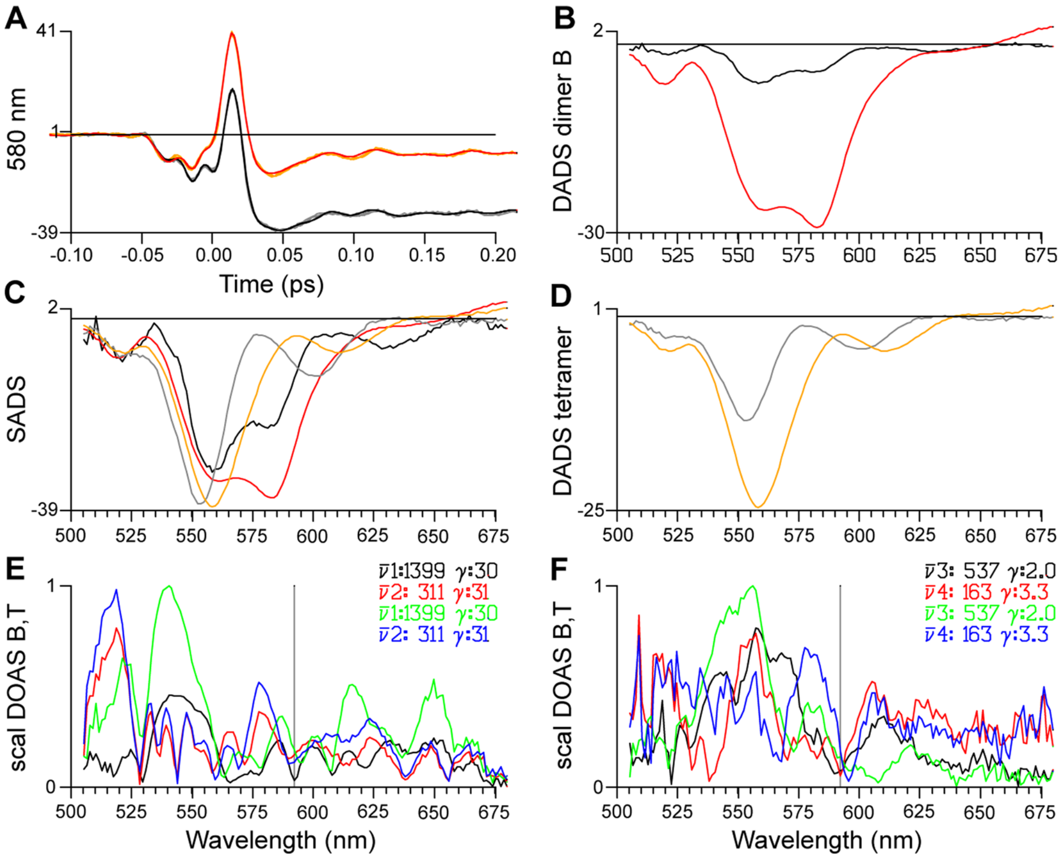

FIG. 3. Simultaneous DOAS analysis of PDI dimer B and the PDI tetramer in chlorobenzene excited with a 15-fs pulse centered at 580 nm and probed with an attenuated pulse. (a) Zoomed-in view from −0.1 ps to 0.2 ps (after the maximum of the IRF) of the 580 nm data (in mOD, gray, dimer B) and the fit (black, dimer B). Orange and red curves depict the tetramer data and fit, respectively. Estimated SADS (c) and DADS [(b) and (d)]. Key dimer B: 313 fs (black) and long lived (red); key tetramer: 478 fs (gray) and long lived (orange). [(e and f)] Estimated DOAS, scaled for comparison. Frequencies $\bar{\nu}n$ (in cm^{-1}) (where n is the DOAS number) and damping rates γ (in ps^{-1}) written in the legend of (e) and (f) using the appropriate color. Key: black and red, dimer B; green and blue, tetramer. The gray vertical lines at 592 nm in (e) and (f) are discussed in the text.

1081 cm^{-1}, 699 cm^{-1}, 418 cm^{-1}, and 259 cm^{-1}.[33,34] The estimated FWHM of the IRF Δ was 15 fs. This ensures that the convolution with the IRF does not average out the damped oscillations with high frequencies. In contrast, the estimated FWHM of the CA IRF Δ' was 34 fs (Fig. S6M, black curve). This cannot be the real IRF width because it would average out the 1399 cm^{-1} (corresponding to a period of 24 fs) damped oscillation that is present in the data.

SADS and DADS

With both dimer B and the tetramer, two lifetimes are needed to describe the data. The estimated DADS of dimer B both represent a decay of bleach plus stimulated emission (SE). The 313 fs DADS [black in Fig. 3(b)] is much smaller than the long-lived DADS [red in Fig. 3(b)]. In the dimer B target model, we assume independent decays with initial populations of 20% and 80%, resulting in the black and red SADS in Fig. 3(c). The bleach near 560 nm is almost the same with the black and red SADS. Note that the long-lived SADS has a stronger bleach plus SE near 585 nm, which is close to the lowest exciton absorption. The long-lived SADS can thus be attributed to the lowest exciton state. Apparently, the Excited State Absorption (ESA) of this state compensates the SE near 620 nm, and above 650 nm, the ESA is larger than the SE. Analogously, the estimated DADS of the tetramer both represent a decay of bleach plus SE. The 478 fs DADS [gray in Fig. 3(d)] is smaller than the long-lived DADS [orange in Fig. 3(d)]. In the tetramer target model, we assume independent decays with initial populations of 36% and 64%, resulting in the gray and orange SADS in Fig. 3(c). Note that both the bleach and the SE of the 478 fs SADS [gray in Fig. 3(c)] are located at higher energy than those of the long-lived SADS [orange in Fig. 3(c)]. Again, the long-lived SADS can be attributed to the lowest exciton state of the tetramer, with a SE band near 610 nm, and ESA next to that. The interpretation of the decay processes of 313 fs and 478 fs will be discussed below.

DOAS and synthesis

The estimated DOAS of the excitonic systems are depicted in Figs. S6D–S6I and compared in Figs. 3(e) and 3(f). The 1399 cm^{-1} oscillation is damped with 30/ps and shows a node in the DOAS near 592 nm in dimer B [black in Fig. 3(e) and black in Fig. S6E], accompanied by a ≈π-phase jump (black in Fig. S6F). The comparison in Fig. 3(e) shows that the tetramer DOAS (green) is larger than the dimer B DOAS (black). The frequency 1399 cm^{-1} is close to that of the 1395 cm^{-1} PDI vibration,[19] and thus, this DOAS can be attributed to vibrational relaxation. The 311 cm^{-1} oscillation is damped with 31/ps, and again, the DOAS is larger in the tetramer (blue) than in dimer B (red). The comparison in Fig. 3(f) shows two weakly damped oscillations of 537 cm^{-1} (damped with 2/ps) and 163 cm^{-1} (damped with 3.3/ps). Again, the DOAS differ, with the tetramer 537 cm^{-1} (green) showing a large broad peak around 550 nm and the dimer B 537 cm^{-1} (black) showing a broad peak extending until 575 nm. This is reminiscent of the differences between the gray and black SADS in Fig. 3(c). The tetramer 163 cm^{-1} DOAS (blue) is larger around 580 nm, but smaller than dimer B (red curve) elsewhere.

Figure S7 demonstrates the decomposition of the 580 nm TA signals. What is very well estimable is the superposition of the CA related signals (IRF and its derivatives, DOAS Nos. 6–11; cf. the orange traces). The 311 cm^{-1} damped oscillations (green traces) are smaller than the CA related signals, but still clearly discernible. They describe the large excursion in the signal between 30 fs and 80 fs. The remaining damped oscillations can only be seen when zooming in (Figs. S7C and S7D). Then, it becomes clear that at 580 nm, the tetramer 537 cm^{-1} and 163 cm^{-1} damped oscillations (magenta and cyan traces) are relatively larger. Decompositions at 40 selected wavelengths are shown in Figs. S8 and S9, confirming the consistency of the DOAS target analysis.

Dimer A

The broadband TA experiment of PDI dimer A in chlorobenzene solution has been performed with pulses centered at 580 nm. The amplitude of the coherent artifact plus damped oscillations is huge, up to 84 mOD [Figs. 4(a) and 4(b), Fig. S10]. The shape of the coherent artifact differs from that in Fig. S3; therefore, the

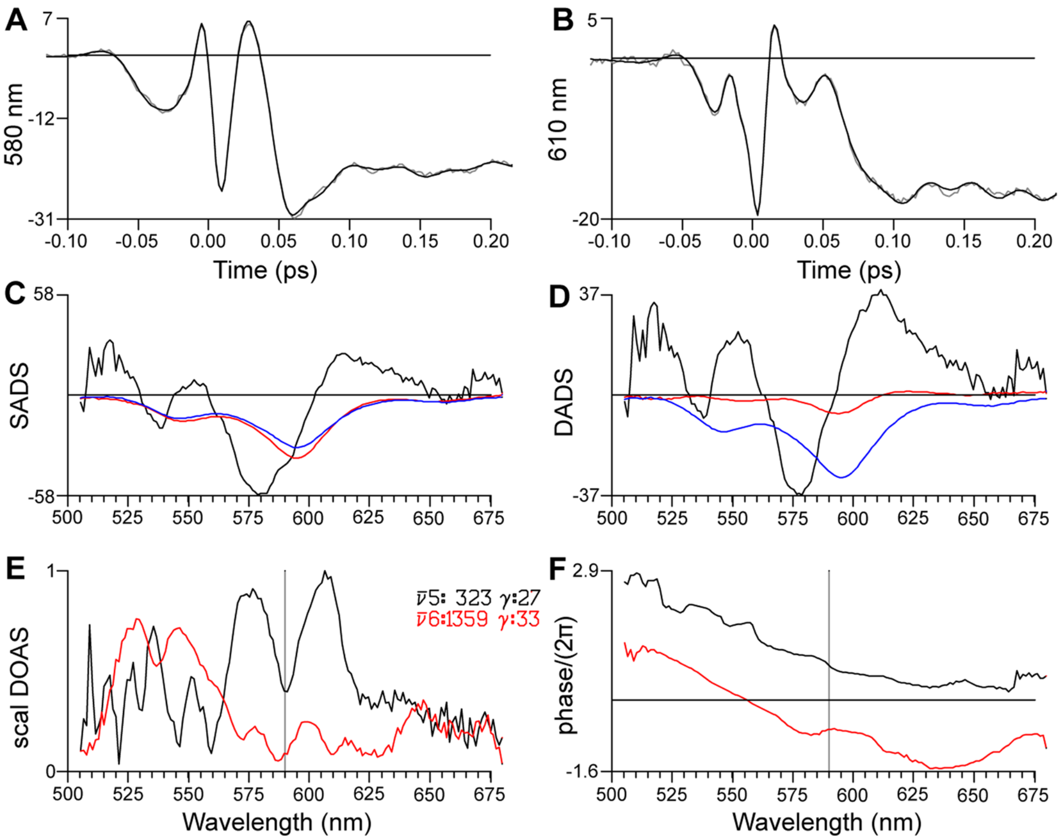

FIG. 4. DOAS analysis of PDI dimer A in chlorobenzene excited with a 15 fs pulse centered at 580 nm and probed with an attenuated pulse. [(a) and (b)] Zoomed-in view from −0.1 ps to 0.2 ps (after the maximum of the IRF) of the 580 nm and 610 nm data (in mOD, gray) and the fit (black). Estimated SADS (c) and DADS (d). Key (c) and (d): 35 (black), 402 fs (red), and long lived (blue). Overview of selected estimated DOAS and phases. Frequencies $\bar{\nu}n$ (in cm^{-1}) (where n is the DOAS number) and damping rates γ (in ps^{-1}) written in the legend of (e) using the appropriate color. (e) Estimated DOAS scaled for comparison. (f) Estimated phase profiles of the DOAS. The gray vertical lines at 591 nm in (e) and (f) are discussed in the text.

dimer A had to be analyzed independently. 11 damped oscillations were needed to fit the vibrational evolution up to the noise level (cf. Figs. S10 and S11). No obvious structure is discernible in the first left and right singular vectors of the residual matrix depicted in Fig. S12.

SADS and DADS

The excited state dynamics can be described by a sequential kinetic scheme 1 (black) → 2 (red) → 3 (blue) with lifetimes of 35 fs and 402 fs, and long lived (Fig. S13A). The first SADS [black in Fig. 4(c)] shows a minimum at ≈580 nm consisting of bleach and early SE, and ESA below 530 nm and from 605 nm to 645 nm. The first DADS [black in Fig. 4(d)] shows negative amplitudes from 565 to 590, indicating the loss of bleach plus SE. Elsewhere, the first DADS is positive, indicating the loss of ESA or gain of SE around 610 nm. The second SADS [red in Fig. 4(c)] shows a broad bleach plus SE around 595 nm and a bleach shoulder near 540 nm. The third SADS is of similar shape as the second, but with a loss in the 595 nm amplitude [cf. the red DADS in Fig. 4(d)]. Alternatively, the second and third DADS could represent parallelly decaying species, like with dimer B, with initial populations of ≈20% and ≈80%.

DOAS and synthesis

An overview of the estimated DOAS and phases is shown in Figs. S13D–S13L, whereas the estimated IRFAS are depicted in Fig. S13N. The undamped first DOAS shows a node at 603 nm, accompanied by a ≈π-phase jump (black in Figs. S13K and S13L). Analogously, undamped DOAS Nos. 2–4 are assigned to ISRS from the chlorobenzene solvent, since 999 cm^{-1} corresponds to a well-known Raman band, and also 699 cm^{-1}, 418 cm^{-1}, and 259 cm^{-1}.[33,34]

DOAS Nos. 7–11 are related to the fitting of the pre-zero oscillations and the CA and will not be discussed further. DOAS No. 5, 323 cm^{-1}, decay rate 27/ps, has the largest amplitudes near 610 nm and 575 nm and could be related to the dimer ES. It is interesting to note that this decay rate of 27/ps is closest to the decay rate of the first ES (35 fs = 29/ps). It shows a node at 590 nm, accompanied by a ≈π-phase jump [black in Figs. 4(e) and 4(f)]. This could indicate the presence of a wavepacket in the ES. DOAS No. 6, 1359 cm^{-1}, decay rate 33/ps, has a frequency close to the 1395 cm^{-1} vibration and could be related to vibrational relaxation.

A complication in the fitting is the collinearity of the strongly damped oscillations with the IRF and its derivatives (Figs. S13D and S13M). Since dimer A had to be analyzed independently, there is no additional information to resolve the CA from the excitonic contributions. Figure S14 demonstrates the decomposition of the 580 nm and 610 nm TA signals. What is very well estimable is the superposition of the CA related signals (IRF and its derivatives, DOAS Nos. 7–11; cf. the orange traces). The 323 cm^{-1} damped oscillation (green traces) is overlapping in time with the later part of these orange traces, which indicates that it must be interpreted cautiously. Compared to the 311 cm^{-1} DOAS in Fig. 3(e), the amplitudes of the 323 cm^{-1} damped oscillations appear to be overestimated between 570 nm and 615 nm. The slowly damped DOAS from Fig. 3(f) could not be resolved with dimer A.

Interpretation

We observe fast and slow dynamics. The fast dynamics in dimer B and the tetramer are the oscillations decaying with ≈30/ps in Fig. 3(e). It can be attributed to vibrational relaxation, since there is excess energy in the pump pulse, which must be dissipated. In dimer A, we also observe this [Fig. 4(e)]. In addition, we observe a 35 fs process [cf. Figs. 4(c) and 4(d)]. Could this be high to low exciton relaxation?[19] That is not very likely, since no rise of the low exciton GSB is observed. Could it be related to solvation? Chlorobenzene has a dipole moment of 1.7 D; thus, one expects to observe solvation. In Ref. 23, solvation time scales of ≈40 fs and ≈150 fs have been observed. Clearly, the SE around 615 nm rises with 35 fs [black DADS, Fig. 4(d)], and thus, it can be attributed to the fast solvation time scale.

The slow dynamics with rates between 2.1 and 3.2/ps is associated with a loss of bleach and SE amplitude [cf. the black and gray DADS in Figs. 3(b) and 3(d) and the red DADS in Fig. 4(d)]. This can be attributed to annihilation in systems that are doubly excited, i.e., decay of the higher energy exciton, while the low exciton state remains populated. Quantitatively, the maximum amplitude of the long-lived DADS is about 30 mOD, which corresponds to 1/8 of the maximum absorption of the sample of 240 mOD. Thus, after the slow dynamics are over, with the dimers about one out of four dimers is still excited, and one out of two tetramers. With the help of the Poisson probability density function, the relative probabilities of systems absorbing one or more photons can be computed. Using a mean rate of 0.42, 80% of the excited dimers absorbs a single photon and 20% absorbs two (or more) photons. With the double rate, 0.84, 64% of the excited tetramers absorbs a single photon and 36% absorbs two (or more) photons. This is in excellent agreement with the initial populations of the target model. The black and gray SADS in Fig. 3(c) can thus be interpreted as the SADS of the one but lowest exciton state of dimer B and the tetramer. In particular, the energy difference between the bleach minima is 768 cm^{-1} for dimer B and 162 cm^{-1} for the tetramer. With dimer A, this is less clear. From the redshift of the maximum emission wavelength relative to that of the PDI monomer (Table I), we have computed the

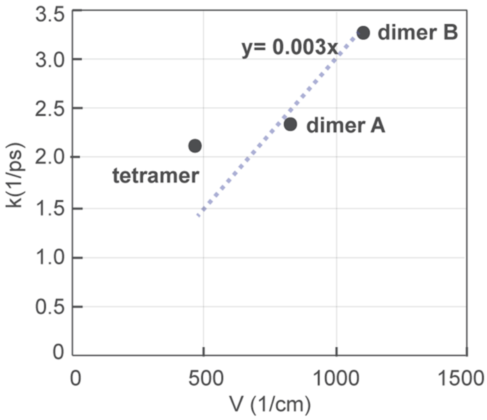

FIG. 5. Annihilation rate vs coupling strength V computed from Table I.

coupling strength V. The annihilation rate is plotted against the thus computed V in Fig. 5, together with a tentative trend line. To further investigate this interesting annihilation process, more experiments with different laser powers combined with solvent measurements would be needed. These can then be corroborated by theoretical computations.[19,35–37]

Decomposition of the SADS and steady state spectra for the tetramer and the monomer

The tetramer has the cleanest exciton effect, since the tetramer has no through-conjugation of the chromophores. Therefore, it is of interest to compare the estimated SADS and the steady state spectra for the tetramer in chlorobenzene. Because the SADS consist of bleach and SE negative contributions, together with a positive ESA contribution, in the overlay Fig. 6, we present the *inverted* SADS. The shape of the first SADS main peak (gray) overlaps with the low energy part of the steady state absorption (black). Probably, the SE contribution to the first SADS overlaps with this main peak, with a vibrational band peaking near 600 nm. At the high energy side, a vibrational shoulder is present near 520 nm. The two peaks are shifted to lower energy in the second SADS (orange), consistent with the interpretation that this represents the lowest exciton state. The SE contribution to the main peak is clearly visible as the difference between the black and orange flanks from 560 nm to 590 nm. The ESA contributions (visible here as negative amplitudes above 640 nm) appear to be small. The energy difference between the maxima of the first and second SADS at ≈552 nm and ≈558 nm corresponds to ≈195 cm^{-1}. The energy difference between the secondary maxima of the first and second SADS at ≈600 nm and ≈610 nm corresponds to ≈262 cm^{-1}. Taking into account the uncertainties and unknown ESA contributions, and the fact that main peak contains both bleach and SE contributions, these numbers are consistent. Since the secondary maxima do not contain a bleach contribution, our estimate based on the inspection of the spectra for the energy difference between the one but lowest and the lowest exciton state is ≈262 cm^{-1}.

To further quantify these observations, we fitted the spectra with Gaussian bands. The absorption and the emission were described by two Gaussian bands. With the absorption, the difference of the location of the maxima was fixed at 1395 cm^{-1} to reduce the number of free parameters. Both the bleach and the SE of the SADS were described by two Gaussian bands, with the difference of the location of the maxima fixed at 1395 cm^{-1}. To further reduce the number of free parameters, the width parameter was linked. The quality of these spectral fits was good (Figs. S15 and S16). The estimated parameters are collated in Table II. The location of the maximum of the main bleach bands is 18 073 cm^{-1} and 18 058 cm^{-1} with SADS 1 and 2, and 18 129 cm^{-1} with the absorption. These differences are considered to be small. The locations of the maximum of the SE bands are 18 058 cm^{-1} and 17 756 cm^{-1} with SADS 1 and 2, and 17 495 cm^{-1} with the emission. The lower $\tilde{\nu}_{\max}$ of the emission is attributed to small wavelength calibration uncertainties between the steady state and broadband spectroscopy. With the SADS (which share a common wavelength calibration), the differences are considered to be significant. Thus, based on the estimated SE bands, our most reliable estimate for the energy difference between the one but lowest and the lowest exciton state is 302 cm^{-1}. The FWHM $\Delta\tilde{\nu}$ of the Gaussian bands is 804 cm^{-1} and 897 cm^{-1} with SADS 1 and 2, and 951 cm^{-1} and 864 cm^{-1} with the main absorption and emission bands. These numbers are quite similar and indicate a large inhomogeneous broadening (disorder)[19] of ≈900 cm^{-1}.

Analogously, the steady state spectra of the tetramer and the monomer in dichloromethane could be well fitted with two Gaussian bands (Fig. S17). The locations of the main peaks of the monomer are higher than those of the tetramer by 94 (absorption) and 203 cm^{-1} (emission) (Table S2), which can be attributed to excitonic effects. The estimated parameters of these fits (Table S2) are consistent with the results in chlorobenzene (Table II). In particular, the FWHM of the main emission band was 933 cm^{-1} and

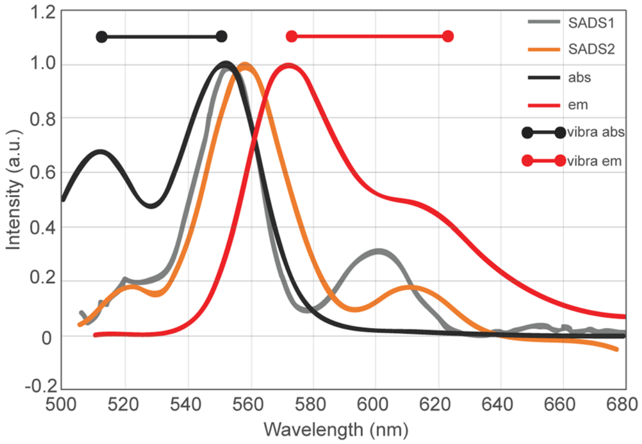

FIG. 6. Overlay of the estimated SADS and the steady state spectra for the tetramer in chlorobenzene. Key: 478 fs (gray) and long lived (orange) inverted SADS; steady state absorption (black) and emission (red) with on top horizontal lines, indicating an energy difference of 1395 cm^{-1} from the location of the maximum.

TABLE II. Location of the maximum $\tilde{\nu}_{\max}(\text{cm}^{-1})$ and full width at half maximum $\Delta\tilde{\nu}(\text{cm}^{-1})$ of the Gaussian bands used to fit the spectra in chlorobenzene. Main bands in bold.

Spectrum	$\tilde{\nu}_{\max}(\text{cm}^{-1})$	$\Delta\tilde{\nu}(\text{cm}^{-1})$
SADS 1 bleach	19 468	804
SADS 1 bleach	**18 073**	**804**
SADS 1 SE	**18 058**	**804**
SADS 1 SE	16 663	804
SADS 2 bleach	19 451	897
SADS 2 bleach	**18 056**	**897**
SADS 2 SE	**17 756**	**897**
SADS 2 SE	16 361	897
Absorption	19 524	1282
Absorption	**18 129**	**951**
Emission	**17 495**	**864**
Emission	16 359	1896

876 cm^{-1} for the tetramer and the monomer, respectively. The FWHM of the main absorption band was 981 cm^{-1} and 903 cm^{-1} for the tetramer and the monomer, respectively. These values are very similar to their counterparts in chlorobenzene, confirming that the inhomogeneous broadening (disorder)[19] is ≈900 cm^{-1}. The facts that the FWHM of the tetramer is larger with the absorption than with the emission (differences of 48 cm^{-1} and 87 cm^{-1} in dichloromethane and chlorobenzene, respectively) and that, in dichloromethane, the absorption FWHM is larger with the tetramer than with the monomer (difference of 78 cm^{-1}) can be explained by contributions from the higher excitonic states to the absorption.

CONCLUSIONS

When two systems have been measured in the same conditions, they can be simultaneously analyzed, thus enhancing the resolvability of the vibronic and excitonic dynamics of the systems. The solvent contributions that are the CA and long-lived ISRS oscillations, which are common in the experiments, can thus be resolved more reliably.

An earlier study on dimer A[19] demonstrated that for this model homodimer system in the strong electronic coupling regime, energy relaxation within the excitonic manifold occurs in the very early (<50 fs) time frame after photoexcitation, precluding the persistence of long-lived coherences between exciton states. Here, we have quantified and detailed that vibrational relaxation as evidenced by the 1399 cm^{-1} or 1359 cm^{-1} damped oscillations occurs with damping rates of ≈30/ps. It was proposed in Ref. 19 that intramolecular degrees of freedom dictate the relaxation rate through radiationless internal conversion pathways. Here, we resolved damped oscillations of 311 cm^{-1} or 323 cm^{-1} with damping rates of ≈30/ps, which might be involved. In dimer A, we found evidence of fast solvation with a rate of 35/ps. A relaxation process with a rate of 2.1/ps–3.2/ps that is positively correlated with the excitonic coupling was discovered in all three model systems. It can be attributed to the annihilation of the one but lowest exciton state. In the tetramer, which has the cleanest exciton effect, the energy difference between the one but lowest and the lowest exciton state is 302 cm^{-1}.

SUPPLEMENTARY MATERIAL

See the supplementary material for additional steady state spectra and figures demonstrating the quality of the fit, the complete analysis, and decompositions.

ACKNOWLEDGMENTS

This work was supported by the Natural Sciences and Engineering Research Council of Canada, DARPA (QuBE) and the United States Air Force Office of Scientific Research Contract No. FA9550-13-1-0005 to G.D.S. and by the research scholarship from the Natural Sciences and Engineering Research Council of Canada and the Ontario Graduate Scholarship to C.C.J. The NCSU portion of this work was supported by the Air Force Office of Scientific Research (Grant No. FA9550-18-1-0331).

There is no conflict of interest to declare.

DATA AVAILABILITY

The data that support the findings of this study are available within the article and its supplementary material.

REFERENCES

[1] R. E. Blankenship, *Molecular Mechanisms of Photosynthesis*, 2nd ed. (Wiley-Blackwell, 2014).

[2] R. Croce, R. van Grondelle, H. van Amerongen, and I. van Stokkum, *Light Harvesting in Photosynthesis* (CRC Press, Boca Raton, 2018), p. 625.

[3] D. Gust, T. A. Moore, and A. L. Moore, "Solar fuels via artificial photosynthesis," Acc. Chem. Res. **42**(12), 1890–1898 (2009).

[4] F. Würthner, "Perylene bisimide dyes as versatile building blocks for functional supramolecular architectures," Chem. Commun. **14**, 1564–1579 (2004).

[5] M. R. Wasielewski, "Self-assembly strategies for integrating light harvesting and charge separation in artificial photosynthetic systems," Acc. Chem. Res. **42**(12), 1910–1921 (2009).

[6] C. Hippius, I. H. M. van Stokkum, E. Zangrando, R. M. Williams, and F. Würthner, "Excited state interactions in calix[4]arene–perylene bisimide dye conjugates: Global and target analysis of supramolecular building blocks," J. Phys. Chem. C **111**(37), 13988–13996 (2007).

[7] C. Hippius, I. H. M. van Stokkum, M. Gsänger, M. M. Groeneveld, R. M. Williams, and F. Würthner, "Sequential FRET processes in calix[4]arene-linked orange-red-green perylene bisimide dye zigzag arrays," J. Phys. Chem. C **112**(7), 2476–2486 (2008).

[8] C. Hippius, I. H. M. van Stokkum, E. Zangrando, R. M. Williams, M. Wykes, D. Beljonne, and F. Würthner, "Ground- and excited-state pinched cone equilibria in calix[4]arenes bearing two perylene bisimide dyes," J. Phys. Chem. C **112**(37), 14626–14638 (2008).

[9] K. E. Brown, B. S. Veldkamp, D. T. Co, and M. R. Wasielewski, "Vibrational dynamics of a perylene–perylenediimide donor–acceptor dyad probed with femtosecond stimulated Raman spectroscopy," J. Phys. Chem. Lett. **3**(17), 2362–2366 (2012).

[10] C. Ramanan, C. H. Kim, T. J. Marks, and M. R. Wasielewski, "Excitation energy transfer within covalent tetrahedral perylenediimide tetramers and their intermolecular aggregates," J. Phys. Chem. C **118**(30), 16941–16950 (2014).

[11] J. D. Schultz, A. F. Coleman, A. Mandal, J. Y. Shin, M. A. Ratner, R. M. Young, and M. R. Wasielewski, "Steric interactions impact vibronic and vibrational coherences in perylenediimide cyclophanes," J. Phys. Chem. Lett. **10**(23), 7498–7504 (2019).

[12] H. van Amerongen, L. Valkunas, and R. van Grondelle, *Photosynthetic Excitons* (World Scientific Publishing, Singapore, 2000).

[13] R. van Grondelle, V. I. Novoderezhkin, and J. P. Dekker, "Modeling light harvesting and primary charge separation in photosystem I and photosystem II," in *Photosynthesis in Silico: Understanding Complexity from Molecules to Ecosystems*, edited by A. Laisk, L. Nedbal, and Govindjee (Springer, The Netherlands, 2009), pp. 33–53.

[14] R. van Grondelle, J. P. Dekker, T. Gillbro, and V. Sundstrom, "Energy transfer and trapping in photosynthesis," Biochim. Biophys. Acta, Bioenerg. **1187**(1), 1–65 (1994).

[15] M. Kasha, H. R. Rawls, and M. A. El-Bayoumi, "The exciton model in molecular spectroscopy," Pure Appl. Chem. **11**(3-4), 371 (1965).

[16] L. Moretti, B. Kudisch, Y. Terazono, A. L. Moore, T. A. Moore, D. Gust, G. Cerullo, G. D. Scholes, and M. Maiuri, "Ultrafast dynamics of nonrigid zinc-porphyrin arrays mimicking the photosynthetic 'special pair'," J. Phys. Chem. Lett. **11**(9), 3443–3450 (2020).

[17] M. Myahkostupov, V. Prusakova, D. G. Oblinsky, G. D. Scholes, and F. N. Castellano, "Structural refinement of ladder-type perylenediimide dimers: A classical tale of conformational dynamics," J. Org. Chem. **78**(17), 8634–8644 (2013).

[18] M. Myahkostupov and F. N. Castellano, "Tetrahedral rigid core antenna chromophores bearing bay-substituted perylenediimides," Tetrahedron **71**(51), 9519–9527 (2015).

[19] C. C. Jumper, J. M. Anna, A. Stradomska, J. Schins, M. Myahkostupov, V. Prusakova, D. G. Oblinsky, F. N. Castellano, J. Knoester, and G. D. Scholes, "Intramolecular radiationless transitions dominate exciton relaxation dynamics," Chem. Phys. Lett. **599**, 23–33 (2014).

[20] P. C. Arpin, D. B. Turner, S. D. McClure, C. C. Jumper, T. Mirkovic, J. R. Challa, J. Lee, C. Y. Teng, B. R. Green, K. E. Wilk, P. M. G. Curmi, K. Hoef-Emden, D. W. McCamant, and G. D. Scholes, "Spectroscopic studies of cryptophyte light harvesting proteins: Vibrations and coherent oscillations," J. Phys. Chem. B **119**(31), 10025–10034 (2015).

[21] S. D. McClure, D. B. Turner, P. C. Arpin, T. Mirkovic, and G. D. Scholes, "Coherent oscillations in the PC577 cryptophyte antenna occur in the excited electronic state," J. Phys. Chem. B **118**(5), 1296–1308 (2014).

[22] I. H. M. van Stokkum, C. C. Jumper, J. J. Snellenburg, G. D. Scholes, R. van Grondelle, and P. Malý, "Estimation of damped oscillation associated spectra from ultrafast transient absorption spectra," J. Chem. Phys. **145**(17), 174201 (2016).

[23] C. C. Jumper, P. C. Arpin, D. B. Turner, S. D. McClure, S. Rafiq, J. C. Dean, J. A. Cina, P. A. Kovac, T. Mirkovic, and G. D. Scholes, "Broad-band pump–probe spectroscopy quantifies ultrafast solvation dynamics of proteins and molecules," J. Phys. Chem. Lett. **7**(22), 4722–4731 (2016).

[24] Y. X. Yan, E. B. Gamble, and K. A. Nelson, "Impulsive stimulated scattering: General importance in femtosecond laser pulse interactions with matter, and spectroscopic applications," J. Chem. Phys. **83**(11), 5391–5399 (1985).

[25] U. Banin, A. Bartana, S. Ruhman, and R. Kosloff, "Impulsive excitation of coherent vibrational motion ground surface dynamics induced by intense short pulses," J. Chem. Phys. **101**(10), 8461–8481 (1994).

[26] S. Ruhman, A. G. Joly, and K. A. Nelson, "Time-resolved observations of coherent molecular vibrational motion and the general occurrence of impulsive stimulated scattering," J. Chem. Phys. **86**(11), 6563–6565 (1987).

[27] M. Maiuri, M. B. Oviedo, M. Koch, M. Myahkostupov, F. N. Castellano, and G. D. Scholes, "Coherent spectroscopy of PDI-based artificial light-harvesting antenna," in *International Conference on Ultrafast Phenomena* (Optical Society of America, Santa Fe, New Mexico, 2016), p. UTu4A.5.

[28] M. Son, K. H. Park, M.-C. Yoon, P. Kim, and D. Kim, "Excited-state vibrational coherence in perylene bisimide probed by femtosecond broadband pump–probe spectroscopy," J. Phys. Chem. A **119**(24), 6275–6282 (2015).

[29] S. A. Kovalenko, A. L. Dobryakov, J. Ruthmann, and N. P. Ernsting, "Femtosecond spectroscopy of condensed phases with chirped supercontinuum probing," Phys. Rev. A **59**(3), 2369–2384 (1999).

[30] I. H. M. van Stokkum, D. S. Larsen, and R. van Grondelle, "Global and target analysis of time-resolved spectra," Biochim. Biophys. Acta, Bioenerg. **1657**, 82–104 (2004).

[31] P. Hamm and M. Zanni, *Concepts and Methods of 2D Infrared Spectroscopy* (Cambridge University Press, 2011).

[32] C. H. B. Cruz, J. P. Gordon, P. C. Becker, R. L. Fork, and C. V. Shank, "Dynamics of spectral hole burning," IEEE J. Quantum Electron. **24**(2), 261–269 (1988).

[33] M. Wahadoszamen, A. Rahaman, N. M. R. Hoque, A. I. Talukder, K. M. Abedin, and A. F. M. Y. Haider, "Laser Raman spectroscopy with different excitation sources and extension to surface enhanced Raman spectroscopy," J. Spectrosc. **2015**, 895317.

[34] C. T. Meneely, C. Y. She, and D. F. Edwards, "Line-shape parameters of the Raman lines of chloro-, bromo-, and iodobenzene," J. Mol. Spectrosc. **39**(1), 73–78 (1971).

[35] A. L. Dobryakov, S. A. Kovalenko, and N. P. Ernsting, "Electronic and vibrational coherence effects in broadband transient absorption spectroscopy with chirped supercontinuum probing," J. Chem. Phys. **119**(2), 988–1002 (2003).

[36] A. L. Dobryakov, S. A. Kovalenko, and N. P. Ernsting, "Coherent and sequential contributions to femtosecond transient absorption spectra of a rhodamine dye in solution," J. Chem. Phys. **123**(4), 044502 (2005).

[37] A. L. Dobryakov and N. P. Ernsting, "Lineshapes for resonant impulsive stimulated Raman scattering with chirped pump and supercontinuum probe pulses," J. Chem. Phys. **129**(18), 184504 (2008).